



## Supplementary Materials for

### **The Role of Surface Oxygen in the Growth of Large Single-Crystal Graphene on Copper**

Yufeng Hao, M. S. Bharathi, Lei Wang, Yuanyue Liu, Hua Chen, Shu Nie, Xiaohan Wang, Harry Chou, Cheng Tan, Babak Fallahazad, H. Ramanarayan, Carl W. Magnuson, Emanuel Tutuc, Boris I. Yakobson, Kevin F. McCarty, Yong-Wei Zhang, Philip Kim, James Hone, Luigi Colombo,\* Rodney S. Ruoff\*

\*Corresponding author. E-mail: r.ruoff@mail.utexas.edu (R.S.R); colombo@ti.com (L.C.)

Published 24 October 2013 on *Science* Express  
DOI: 10.1126/science.1243879

#### **This PDF file includes:**

Materials and Methods  
Supplementary Text  
Figs. S1 to S12  
References (32–45)

## Materials and Methods

### Cu foil pretreatment, graphene growth and transfer

Commercially available Cu foils, both OF-Cu (Alfa-Aesar stock #42972, #46986, etc.) and OR-Cu (Alfa-Aesar stock #46365, #13382, etc.), have native surface oxide layers and other impurities. In order to remove the surface oxide and contaminants, Cu foils were chemically etched in acetic acid ( $\text{CH}_3\text{COOH}$ ) for 8 hours followed by blow-drying with nitrogen gas. Electrochemical polishing of Cu can also clean the surface and have similar growth results.

Graphene growth was carried out in a low pressure CVD (LPCVD) system. After cleaning, the Cu foils were made into the form of pockets and loaded into the growth system within 5 min to avoid surface oxidation. The system was then heated to 1035 °C under a  $\text{H}_2$  flow of 10  $\text{cm}^3$  per min (sccm), corresponding to  $1 \times 10^{-1}$  Torr, and annealed for 20-100 min;  $\text{CH}_4$  was then introduced into the system for graphene growth. The typical  $P_{\text{CH}_4}$  ranged from  $1 \times 10^{-3}$  to  $5 \times 10^{-2}$  Torr, and the growth time was varied from 10 to 800 min. For  $\text{O}_2$ -assisted growth, pure  $\text{O}_2$  was used before growth for exposure time ranging from 10s to 5 min, and a corresponding  $P_{\text{O}_2}$  is  $1 \times 10^{-3}$  Torr. After growth, the system was cooled down to room temperature while still under the  $\text{H}_2$  and  $\text{CH}_4$  flow. The typical graphene growth procedure is schematically shown in Fig. S1. Note that, during  $\text{O}_2$  exposure, the  $\text{H}_2$  flow can be either “on” or “off”, with the same graphene growth results, i.e., low nucleation density and dendritic domain shapes. The graphene domains/films formed on the inner surface of the Cu pockets were characterized and analyzed.

The graphene domains/films were transferred onto dielectric substrates,  $\text{SiO}_2/\text{Si}$  or h-BN, using a poly(methyl methacrylate) (PMMA)-assisted method (32) for Raman characterizations and electrical device fabrications. Prior to transfer, the graphene surface was spin-coated with a layer of PMMA to provide mechanical support for the graphene throughout the transfer process. The Cu/graphene/PMMA stack was then floated over an ammonium persulfate ( $(\text{NH}_4)_2\text{S}_2\text{O}_8$ , 0.5 M, Sigma Aldrich) aqueous solution to etch the Cu. The resulting graphene/PMMA membranes were thoroughly rinsed with deionized water, and then transferred onto target substrates. The PMMA was removed with acetone, and then rinsed in isopropanol, finally blow dried with nitrogen gas.

## Supplementary Text

### Control experiments and analyses used to confirm the effect of oxygen

#### (1) TOF-SIMS measurements

The presence of oxygen and its stability on the Cu surface under the LPCVD conditions was investigated by  $^{18}\text{O}$ -labeling. This method can exclude the oxygen signals from unintentional oxidation of Cu surface during sample transfer from growth system to analysis system. Briefly, OF-Cu was loaded in the CVD system and heated to 1000 °C under  $\text{H}_2$  gas, then the Cu was exposed to  $^{18}\text{O}_2$  gas for 5 min at  $P_{\text{O}_2}=1 \times 10^{-3}$  Torr followed by annealing in  $\text{H}_2$  ( $P_{\text{H}_2} \sim 0.1$  Torr)

for another 50 min. After cooling, the Cu was transferred from CVD system to TOF-SIMS instrument for analysis. The surface  $^{18}\text{O}$  concentration (mass peak intensity) for low pressure annealing is more than an order of magnitude higher than that of natural abundance of  $^{18}\text{O}$  (Fig. S2A and inset). This experiment shows that surface oxygen species exist and cannot be completely removed in the LPCVD conditions.

In addition, TOF-SIMS depth profiles show that, after  $\text{O}_2$  exposure and annealing in  $\text{H}_2$ , the oxygen concentration in the OF-Cu (O) bulk is approaching  $\sim 10^{-6}$  at.% (the detection limit), as shown in Fig. S2B, which is similar to OF-Cu and annealed OR-Cu. The TOF-SIMS measurements confirm that, at graphene growth temperatures, oxygen species mainly exist on the Cu surface, not in the bulk of the Cu foil.

In each of the following growth, numbered (2)-(4), OF-Cu and OR-Cu were placed side-by-side in the growth system, so that the growth conditions were the same.

(2) Low  $P_{\text{H}_2}$  annealing and then growth.

Both substrates were annealed in low pressure  $\text{H}_2$  (flow rate: 10sccm, pressure: 0.1 Torr) at 1035  $^\circ\text{C}$  for 30 min, and then  $\text{CH}_4$  (flow rate: 0.5sccm, pressure:  $5 \times 10^{-3}$  Torr) was added. The resulting graphene domain shapes were: ‘multi-branched’ on OR-Cu and ‘compact’ on OF-Cu, as shown in Fig. S3A and S3B.

(3) High  $P_{\text{H}_2}$  annealing and then growth.

High pressure  $\text{H}_2$  (flow rate: 1000 sccm, pressure: 10 Torr) annealing at 1035  $^\circ\text{C}$  for 60min, followed by exposure to  $\text{CH}_4$  ( $5 \times 10^{-3}$  Torr) and  $\text{H}_2$  (0.1 Torr) for 30 min. Dense and compact domains were observed on both OR-Cu and OF-Cu, as shown in Fig. S3C and S3D. This high pressure  $\text{H}_2$  annealing is thus considered to completely remove surface oxygen species, eliminating the effect of oxygen.

(4) Exposure to  $\text{O}_2$  gas prior to growth.

$\text{H}_2$  (0.1~10 Torr) annealing was performed at 1035  $^\circ\text{C}$  for 30 min, and then  $\text{O}_2$  exposure ( $1 \times 10^{-3}$  Torr) for 20 s, after which  $\text{H}_2$  (0.1 Torr) and  $\text{CH}_4$  ( $5 \times 10^{-3}$  Torr) were introduced for 30 min. Multi-branched graphene domains were observed on both OR-Cu and OF-Cu, as shown in Fig. S3E and S3F.

It is known that graphene grows on Cu by a surface-mediated process (12). Therefore, chemical specie(s) on the Cu surface were considered as candidate(s) for the domain shape effect. From the above experimental comparisons, oxygen either segregated out of OR-Cu bulk or introduced by  $\text{O}_2$  exposure was found strongly relevant to the observed density of nuclei and domain shapes. We therefore concluded that surface oxygen plays a critical role in the nucleation and growth of graphene on Cu.

In literature, the compact domain growth in an atmospheric pressure CVD process (29), where the  $P_{\text{H}_2}$  is much higher than in LPCVD, is thus also understandable.

### (5) Cu foil tube vs. Cu foil pocket

Previous works (33) show that graphene crystals with a domain size of about 2 mm can be grown on the inner surface of a Cu tube (a Cu foil is rolled into a cylinder with a given diameter). Here, both OF-Cu and OR-Cu pockets and tubes were used to grow graphene under the same growth conditions. Typical geometry for the tube is 5 cm in length and 5 mm in diameter and the growth conditions were:  $P_{H_2}=0.1$  Torr and  $P_{CH_4}=1 \times 10^{-3}$  Torr. The exposure time to  $CH_4$  was 3.5 hours for OR-Cu, and 40 min for OF-Cu. As shown in Fig. S4. The primary difference in the domain size and shape in the experiments is only due to the presence of oxygen, not sample geometry.

### Optical images and Raman spectra of graphene domains

A 488 nm excitation laser with a 100  $\times$  objective lens in WITec Alpha 300 micro-Raman imaging system was used for acquisition of Raman spectra and maps of the graphene domains/films.

Both compact and dendritic graphene domains were transferred onto Si substrates with 285nm thick thermal oxide, as shown in Fig. S5A-S5D. The uniform brightness and contrast in optical images suggest that the domains have a uniform thickness. The Raman spectra show that the domains are single-layer graphene with weak D peaks present only at the edges of domains. In addition, small multi-layer regions were found near the center of the large graphene domains, as shown in the optical image of Fig. S5C, and also evidenced by a broader Raman 2D peak (Fig. S5E) (34). The multi-layer area was less than 1% of the total domain area.

### Raman mapping and area growth rate calculations

The area growth rate (coverage rate,  $d\theta/dt$ ) of graphene films on Cu can be obtained from carbon isotope-labeled growth and Raman mapping. As shown in Fig. S6A and S6B, the Raman 2D (also referred to as G') peak intensity maps of continuous graphene films on both OF-Cu and OF-Cu (O) reveal the progress of the growth process until full coverage. The growth conditions:  $P_{CH_4}=2 \times 10^{-3}$  Torr (flow rate: 0.2 sccm),  $T=1035$   $^{\circ}C$ , growth time 90 min for OF-Cu, and 180 min for OF-Cu (O),  $O_2$  exposure at  $1 \times 10^{-3}$  Torr for 30s. The surface coverage ( $\theta$ ) can thus be extracted from the maps and plotted as a function of growth time (Fig. S6C, left plots). The plot from OF-Cu (O) was calculated with an area greater than  $500 \mu m \times 500 \mu m$  to avoid any local non-uniformity in  $\theta$ . The  $\theta$  in both cases are non-linear, as shown in the left plots of Fig. S6C. The time to full surface coverage in the case of OF-Cu (O) is found to be twice as long as that on bare OF-Cu. Moreover, at any time of growth, coverage on OF-Cu is always higher than that on OF-Cu (O). This is reasonable since the low nucleation density on OF-Cu (O) leads to low  $\theta$ .

To further elucidate this, simple calculations were carried out. As shown in Fig. 3A, 3B, and Fig. S6, the samples were grown on either OF-Cu or OF-Cu (O) under the same conditions. The nucleation density,  $N$ , is  $\sim 6 \times 10^{-3} \mu\text{m}^{-2}$  for OF-Cu, more than two orders of magnitude higher than that for OF-Cu (O),  $\sim 2 \times 10^{-5} \mu\text{m}^{-2}$ . The radial growth rate,  $d\bar{r}/dt$  (defined below), for OF-Cu is about 10 times lower than that for OF-Cu (O) during the first 32 minutes. According to the relation:  $N \times \bar{r}^2 \propto \theta$ , the coverage,  $\theta$ , for OF-Cu case is therefore higher than that for OF-Cu (O), consistent with our experimental results for the first 32 min growth (Fig. S6C). To summarize, low  $N$  leads to low  $\theta$  even though the radial growth rate of individual domains is higher due to oxygen.

The corresponding  $d\theta/dt$  is obtained by differentiating the surface coverage with respect to time, as shown in Fig. S6C (plots on the right). Two stages, accelerating and then decelerating growth, are observed in both cases (OF-Cu and OF-Cu (O)). In the early growth stage, the distance between neighboring graphene domains is larger than the diffusion length of carbon species, so that the growth of any single domain is not influenced by the existence of the others, and  $d\theta/dt$  increases with domain edge length, i.e., domain perimeter. Later, at the decelerating stage, each domain grows under the influence of its neighbors, and the  $d\theta/dt$  is thereby decreased until full coverage, a typical example being the blue rectangle in Fig. S6B. In the main text, the calculation and analysis of individual domain growth rates are limited to the early growth periods, in which the growth is free of inter-domain competition.

#### Activation energy calculations

Before inter-domain competition occurs, the radial growth rates ( $dr/dt$ ) of individual graphene domains are nearly constant along a given crystal orientation, as revealed by isotope-labeled growth in Fig. S7A-7J. We can therefore investigate radial growth rates of individual domains as a function of temperature. In this work, we used the average radial growth rate  $d\bar{r}/dt$  and ignored the crystal orientation effect. As illustrated in Fig. S7K, individual graphene domains with different shapes are converted into circular shapes of the same area. Because of the nearly constant radial growth rate, the circular shapes can also be drawn as concentric circles with equidistant radii (the radial lengths at given time spans). The corresponding radial growth rate is defined as  $d\bar{r}/dt$ .

#### Low energy electron microscopy, photoelectron emission microscopy, and low energy electron diffraction

Low energy electron microscopy (LEEM), photoelectron emission microscopy (PEEM), and low energy electron diffraction (LEED) were performed using an Elmitec LEEM III instrument. The as-grown graphene samples were transferred and loaded into the LEEM instrument, and then degassed at 250 °C overnight in ultra-high vacuum (base pressure  $< 2 \times 10^{-10}$  Torr). The measurements were taken at room temperature. A Hg lamp (energy  $< 5$  eV) was used to generate

the PEEM images, whose field of view (normally 140  $\mu\text{m}$ ) is greater than the largest field of view available in LEEM (about 75  $\mu\text{m}$ ). Selected-area LEED was typically obtained from 2  $\mu\text{m}$ -diameter regions of the surface.

Fig. S8 shows a graphene domain growing across Cu multi-grains and corresponding LEEM image and LEED patterns from different regions of the domain. The seven aligned LEED patterns conclude that the domain is a single-crystal.

## Phase field simulations

### (1) Simulation method summary

In a phase-field model (35,36), an order parameter (phase field) varies smoothly between multiple phases with a diffused interface of finite width. In this simulation of graphene growth patterns, the phase-field model consists of an order parameter  $\psi$  and a concentration field  $\xi$ . On the Cu substrate, the order parameter  $\psi = -1$  and on the graphene layer  $\psi = 1$ . For the concentration  $u$  of the carbon species arriving on the Cu substrate, the field is  $\xi = \Gamma(u - u_{eq})$ , where  $\Gamma$  is the atomic area of the solid and  $u_{eq}$  is the equilibrium concentration of the carbon species on the surface. The free energy functional  $G$  is based on that given by Karma and Plapp (37) and can be expressed as:

$$G = \oint \kappa^2 (\nabla \psi)^2 - \frac{1}{\pi} \cos(\pi[\psi - \psi_0]) + \varphi \xi \left\{ \psi + \frac{1}{\pi} \sin(\pi[\psi - \psi_0]) \right\} \quad (1)$$

The growth equations for  $\psi$  and  $\xi$  are written as:

$$\tau_\psi \frac{\partial \psi}{\partial t} = - \frac{\delta G}{\delta \psi} \quad (2)$$

$$\frac{\partial \xi}{\partial t} = D \nabla^2 \xi - \frac{\xi}{\tau_s} + F - \frac{1}{2} \frac{\partial \psi}{\partial t} \quad (3)$$

$\kappa^2$  is the gradient energy term and the anisotropy of the graphene step energy is included in this term as  $\kappa^2 = k^2 \{1 + \varepsilon_g \cos(n\theta)\}$ , where  $k^2$  is the constant average interface energy density,  $\varepsilon_g$  is the strength of the anisotropy and  $n$  corresponds to the symmetry. We use  $n=6$  for six-fold anisotropy. The characteristic time of attachment of the carbon species is  $\tau_\psi$ , the mean life time of the species on the surface is  $\tau_s$  with  $\tau_\psi < \tau_s$ . The flux of the carbon species arriving at the surface is  $F$ ,  $\varphi$  is a dimensionless coupling constant and  $D$  is the diffusion coefficient of the carbon species. The minima of the free energy  $G$  are at  $\psi - \psi_0 = 2m + l$ , where  $m$  is an integer, and are independent of  $\xi$ . The growth morphology of graphene is controlled by the competition among a few parameters, such as the characteristic time of attachment  $\tau_\psi$ , the flux  $F$  and the diffusion coefficient  $D$  ( $D$  is fixed in this work), but its symmetry is controlled by the graphene edge energy, that is, six-fold on Cu(111).

We solve the evolution equations for the order parameter  $\psi(x, y, t)$  and concentration field  $\xi$  (Eqs. 2-3) using the discrete Fourier transform method (38) with periodic boundary conditions in the in-plane ( $x$  and  $y$ ) directions. The length and time are scaled in phase-field units (35,36), i.e.,

length using  $\kappa^2=1$  and time is measured in units of  $\tau_\psi$ . Using  $\Delta x = \Delta y = 1$  and  $\Delta t = 0.01$ , the equations are discretized in both space and time and the system cell sizes are  $256 \times 256$  for Fig. S9A,  $512 \times 512$  for Fig. 4J, 4K and Fig. S9C, 9E, and  $1024 \times 1024$  for Fig. 4L. The other parameters used are  $D = 6$ ,  $k^2 = 2$ ,  $\varepsilon_g=0.01$ ,  $u_{eq} = \xi(x, y, 0) = 0.5$ ,  $\tau_s = 1000000.0$  and  $\varphi = 10$ . We start with a circular nucleus of radius 10. We carry out simulations at different values of  $F$  and  $\tau_\psi$  and compare with the experiments.

(2) Domain shape diversity from changes in carbon flux ( $F$ ) and characteristic attachment time ( $\tau_\psi$ ).

It should be noted that when an extremely low  $F$  is applied, the simulated domain shape can approach multi-branched (Fig. S9C) with a long  $\tau_\psi$  (high edge attachment barrier). On the other hand, when  $\tau_\psi$  increase from 1.0 to 1.25, the domain shape changes from a dendritic shape (Fig. 4K, 4L) to a less compact one (Fig. S9E). Indeed, it is possible to achieve such transitional domain shapes between edge-attachment limited and diffusion-limited regimes experimentally when either very low  $P_{CH_4}$  on pristine OF-Cu or shorter  $O_2$  exposure (5-10 s) is applied, as shown in Fig. S9D and 9F. The experimental results and simulated patterns agree well with each other. It should be noted that the diversity of graphene domain shapes is the result of the interaction of various parameters, such as  $P_{H_2}$ , surface oxygen species concentration, and carbon flux ( $P_{CH_4}$ ) (30).

### Density Functional Theory calculations

Density functional theory (DFT) calculations are performed with the Vienna *ab initio* Simulation Package (VASP) (39,40) using ultrasoft pseudopotentials (41,42) for electron-ion interactions and the Ceperley–Alder (43) local density approximation (LDA) for the exchange-correlation functional. Here we use LDA in order to describe the weak binding between the graphene basal planes and Cu (it is known that GGA gives non-positive binding (44)). The supercell for modeling the graphene edge is shown in Fig. S10. A graphene ribbon is put onto a double layer Cu(111) slab, with the bottom layer fixed in the surface normal direction. One side of the graphene edge is docked onto the metal and the other side is used to model the growth front (domain edge). Vacuum spacing is kept larger than 15 Å in the direction perpendicular to the metal surface. All structures are fully relaxed until the force on each atom is less than 0.01 eV/Å. A 1 x 11 x 1 Monkhorst–Pack (MK) (45) k-points mesh is used to sample the Brillouin zone.

Since graphene and Cu(111) have a lattice mismatch of ~4%, we use two sets of supercell size: one is based on the lattice parameter of graphene, and the other is based on that of Cu(111). The corresponding energies are shown in Fig. 3I as the upper and lower limits of the bar.

To model H and OH species on Cu(111), we use a 6×6 metal slab with 5 layers. The bottom layer is fixed in the surface normal direction. 5×5×1 MP k-points are used. Both H and OH favor the hollow site of the surface.

The energy of Hydrogen shown in Fig. 3I is defined as:

$E(H@X) = E(H+X) - E(X) - E(H_2)/2$ , where X can be H<sub>2</sub>, the Cu(111) surface, the graphene edge (G edge), etc.  $E(H+X)$  is the total energy of the system which contains both H and X,  $E(X)$  is the energy of X without H, and  $E(H_2)$  is the energy of H<sub>2</sub> molecule.

When O<sub>2</sub> exposure was carried out in an H<sub>2</sub> environment (Fig. S1), H<sub>2</sub>O molecules may potentially form on the Cu surface. The DFT calculation results showed that the reaction,  $H_2O \xrightarrow{Cu} H + OH$ , is energetically possible. However, DFT calculations show that the OH group does not promote graphene edge dehydrogenation in the proposed reaction:  $CH_x + OH \xrightarrow{Cu} CH_{x-1} + H_2O$  ( $x=4, 3, 2, 1$ ). This is contrary to the observed barrier lowering in our experiments (Fig. 3G). Therefore, the (possible) formation of H<sub>2</sub>O or OH on the Cu surface is considered to be of little importance for graphene edge dehydrogenation and large domain growth.

### Electrical transport measurements

The graphene domains were transferred onto SiO<sub>2</sub>/Si or h-BN substrates for electron transport measurements by using the same transfer method as used for Raman characterizations. For the electrically characterized samples, standard electron-beam lithography, reactive ion etching, and physical vapor deposition processes were used to pattern the graphene samples into the Hall bar geometry with Cr/Pd/Au electrodes. After device fabrication, the graphene/h-BN samples were annealed in a tube furnace under a forming gas atmosphere for 6.5 hours at 340 °C. The completed Hall bar devices were imaged with atomic force microscopy (AFM) using silicon cantilevers operating in non-contact mode (Fig. S12A). Samples were cooled in a variable temperature (1.7K–300 K) liquid <sup>4</sup>He flow cryostat with samples in He vapor. Transport measurements were acquired in a four-terminal geometry using a standard lock-in technique at 17 Hz.

The electrical transport properties (Fig. S11) of graphene devices on SiO<sub>2</sub>/Si substrates demonstrate quality comparable to those of exfoliated graphene. The extracted carrier mobility (18) is 10,800 cm<sup>2</sup>V<sup>-1</sup>s<sup>-1</sup> and 8,400 cm<sup>2</sup>V<sup>-1</sup>s<sup>-1</sup> at 4.2K and room temperature, respectively.



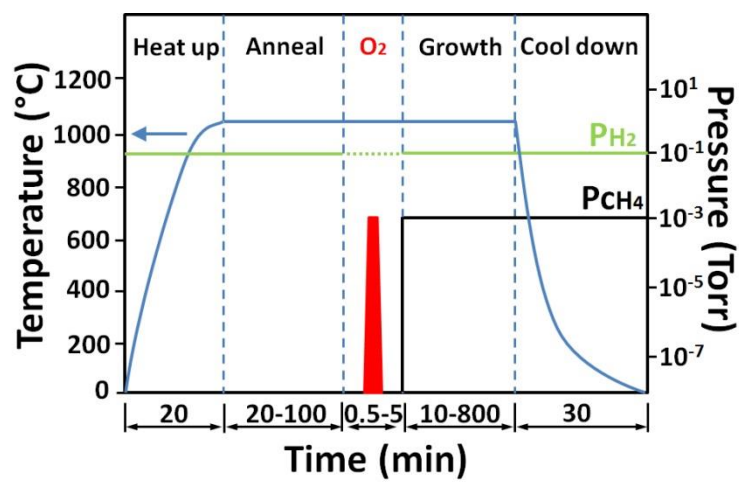


**Fig. S1.**

Schematic of a typical CVD graphene growth process that includes O<sub>2</sub> exposure.

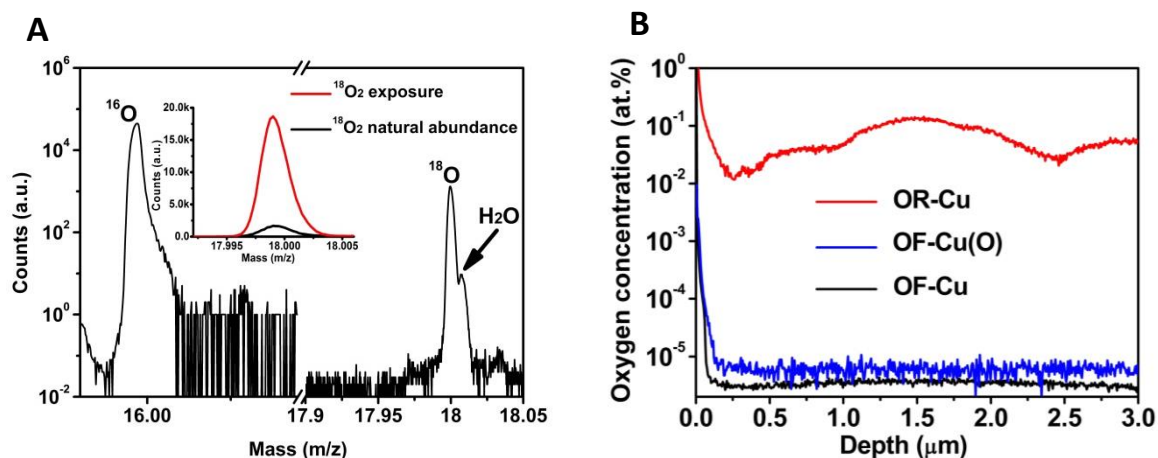


**Fig. S2.**

(A) TOF-SIMS surface measurements of an OF-Cu substrate after  $^{18}\text{O}_2$  exposure and annealing in  $\text{H}_2$ . Inset: The  $^{18}\text{O}$  surface concentration is more than one order of magnitude higher than natural abundance of  $^{18}\text{O}$ . The latter is measured from another Cu substrate without  $^{18}\text{O}_2$  exposure. In the two curves, the  $^{16}\text{O}$  peaks are scaled to have the same intensities. (B) TOF-SIMS depth profiles of oxygen concentration in OR-Cu, OF-Cu, and OF-Cu (O), respectively.

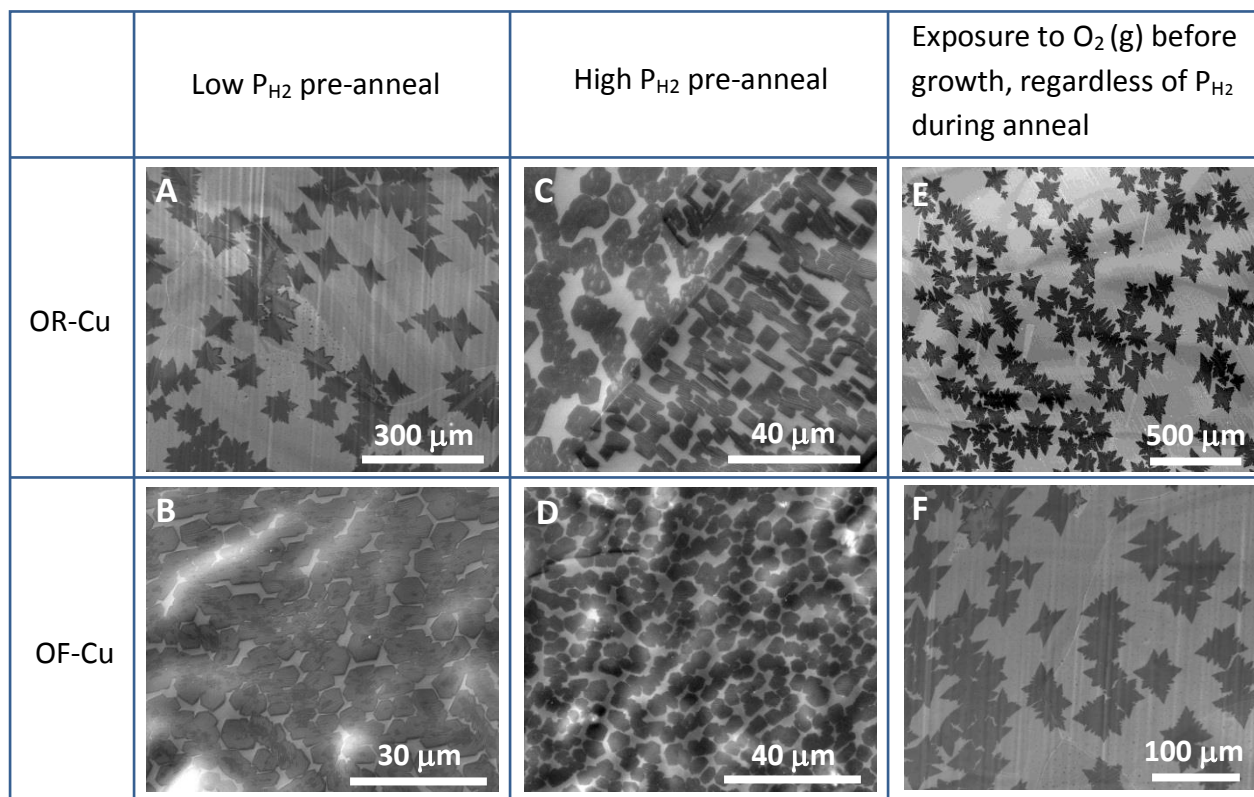


**Fig. S3.**

Growth results of graphene under different Cu substrates and annealing conditions. The growth parameters are the same:  $P_{CH_4}=5 \times 10^{-3}$  Torr,  $P_{H_2}=0.1$  Torr,  $T=1035$  °C, growth time 30 min. Note that, in (E) and (F), the  $P_{H_2}$  is 0.1 Torr before exposure to  $O_2$  gas.

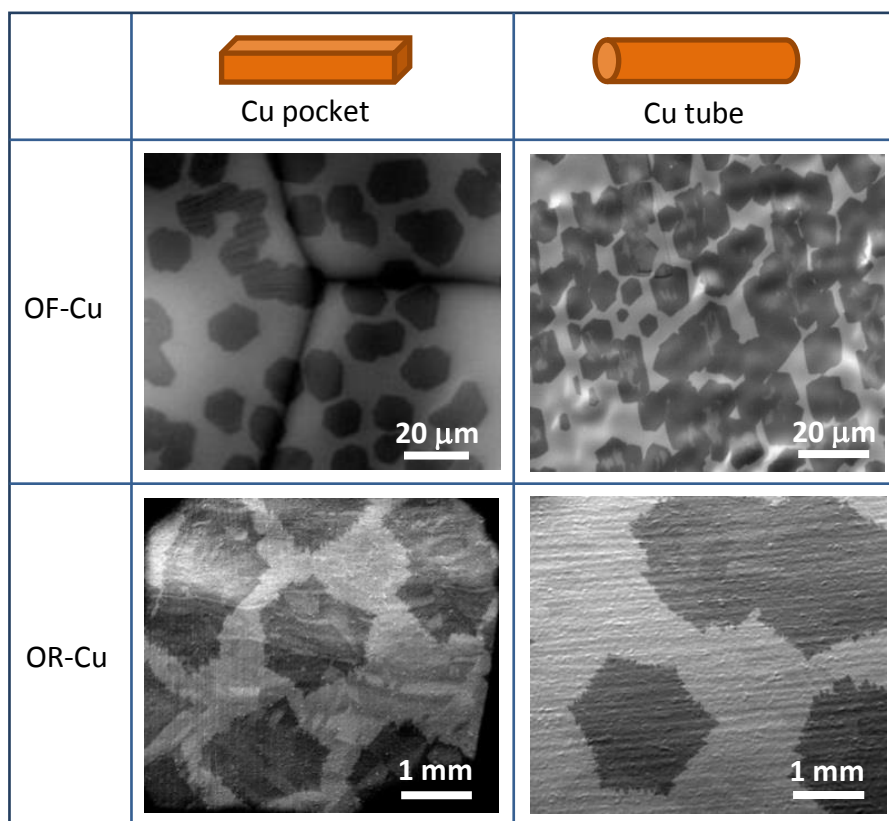


**Fig. S4.**

Growth result comparison between inner surface of Cu pocket and inner surface of Cu tube under the same growth conditions.

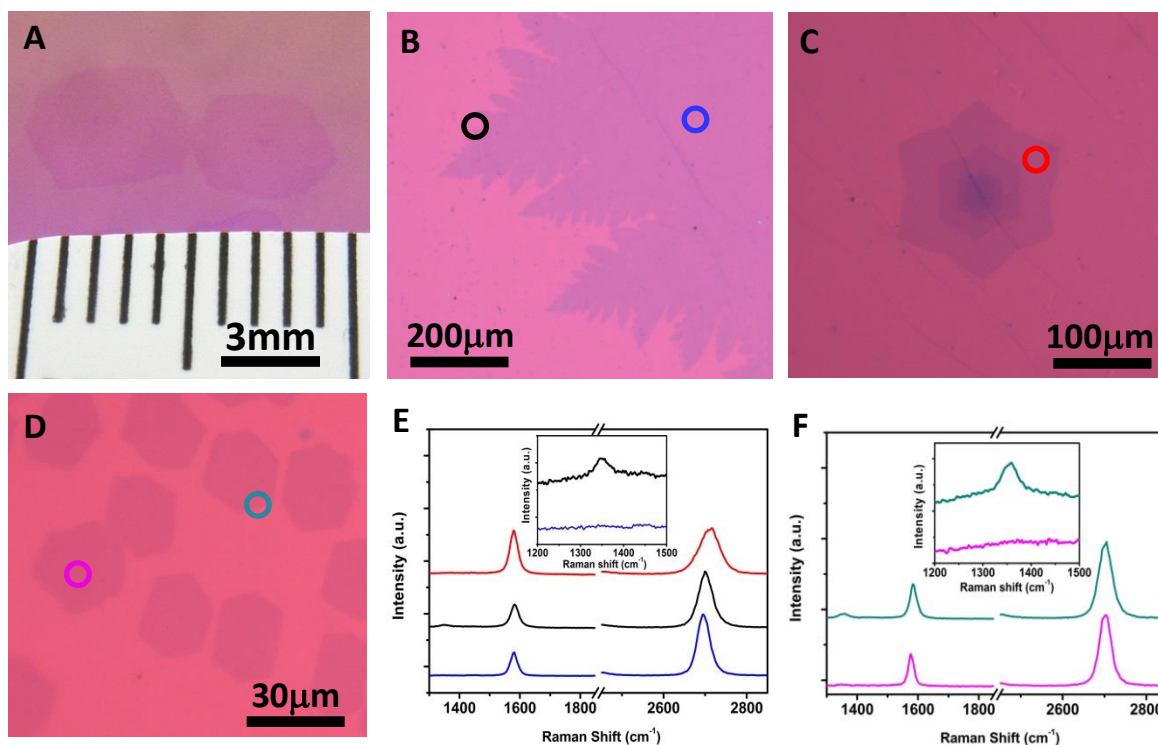


**Fig. S5.**

Optical images and Raman spectra of large-dendritic and small-hexagonal graphene domains. (A-C) the optical images of large graphene domains, domain edge, and domain center on SiO<sub>2</sub>/Si substrates, respectively. (D) Optical image of compact hexagonal domains. (E) Raman spectra at different positions (open circles of different colors) of large graphene domains. Inset is the comparison of D peaks from the inner and edge positions of the domain. (F) Raman spectra at different positions (open circles of different colors) of compact graphene domains. Inset is the comparison of D peaks from the inner and edge positions of the domains.

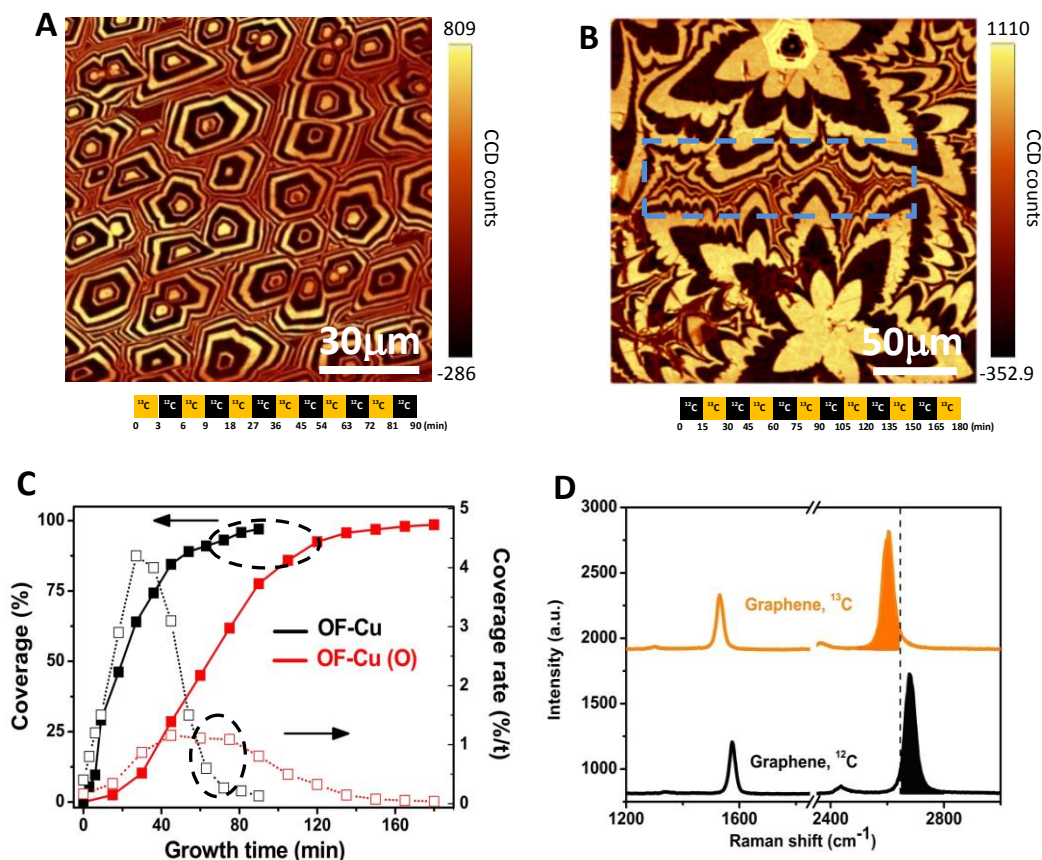
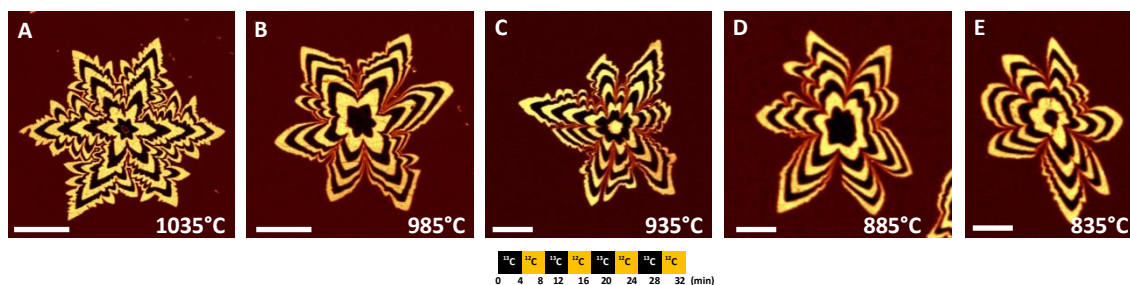


**Fig. S6.**

(A and B) Raman 2D band intensity maps of graphene films grown on OF-Cu and OF-Cu (O), respectively. The blue dashed box in (B) highlights the region corresponding to decelerating growth. (C) The surface coverage (solid lines) and surface coverage rate (dashed lines) on OF-Cu and OF-Cu (O), respectively, as a function of growth time at  $P_{\text{CH}_4} = 2 \times 10^{-3}$  Torr. (D) Raman spectra of graphene with  $^{12}\text{C}$  (normal  $\text{CH}_4$  was used) or  $^{13}\text{C}$ , and illustrate that the Raman maps are from the intensity of the 2D bands, as indicated with the filled areas. The orange and black correspond to the bright and dark areas, respectively, in the Raman maps.



## OF-Cu (O)



## OF-Cu

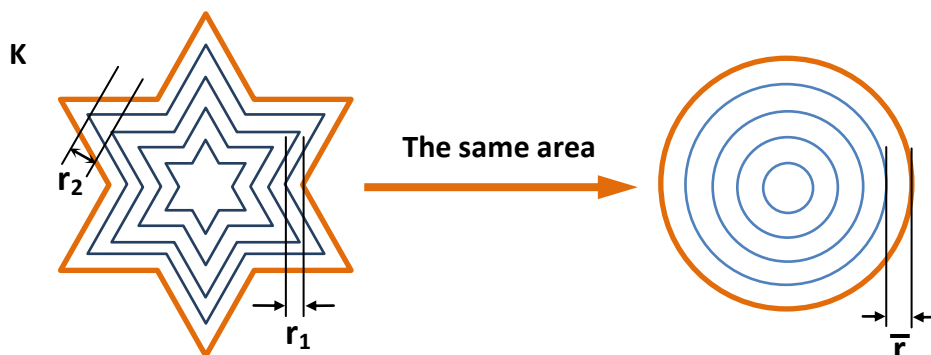
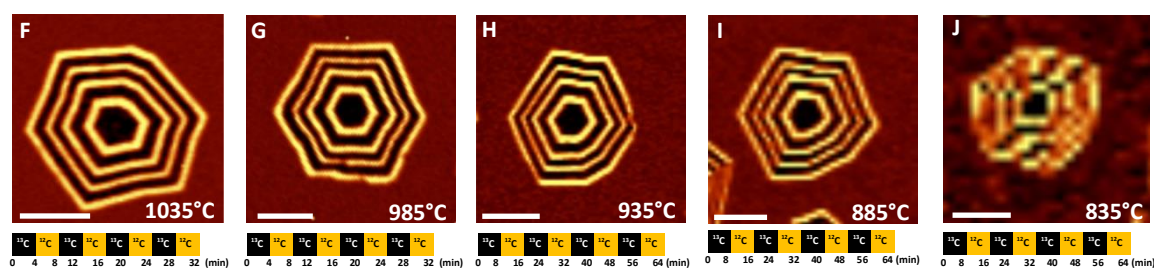


**Fig. S7.**

(A-E) Raman 2D band intensity maps of graphene domains grown on OF-Cu (O) under the same conditions except the temperature. (F-J) Raman 2D band intensity maps of graphene domains grown on the OF-Cu surface, and the isotope intervals are indicated under each image. The growth parameters:  $P_{\text{CH}_4}=2 \times 10^{-3}$  Torr,  $P_{\text{H}_2}=0.1$  Torr,  $\text{O}_2$  exposure at  $1 \times 10^{-3}$  Torr for 30 s in (A-E). Scale bars are: (A)  $30 \mu\text{m}$ , (B)  $20 \mu\text{m}$ , (C)  $15 \mu\text{m}$ , (D)  $9 \mu\text{m}$ , (E)  $8 \mu\text{m}$ , (F)  $5 \mu\text{m}$ , (G)  $3 \mu\text{m}$ , (H)  $2.5 \mu\text{m}$ , (I)  $2 \mu\text{m}$ , and (J)  $0.8 \mu\text{m}$ . (K) Illustration of calculation method to achieve average radial growth rate of graphene domains with different shapes.

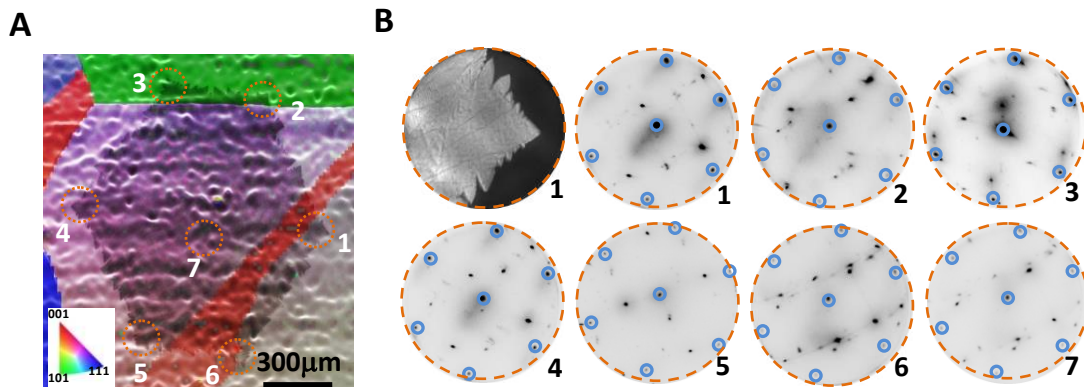


**Fig. S8.**

(A) Superimposed SEM and EBSD image of a graphene domain grown across Cu multi-grains.  
 (B) One LEEM image and seven LEED patterns taken from the regions marked with dash-line circles and numbers 1-7 in (A). The graphene spots are circled in blue. The additional spots come from the faceted Cu.



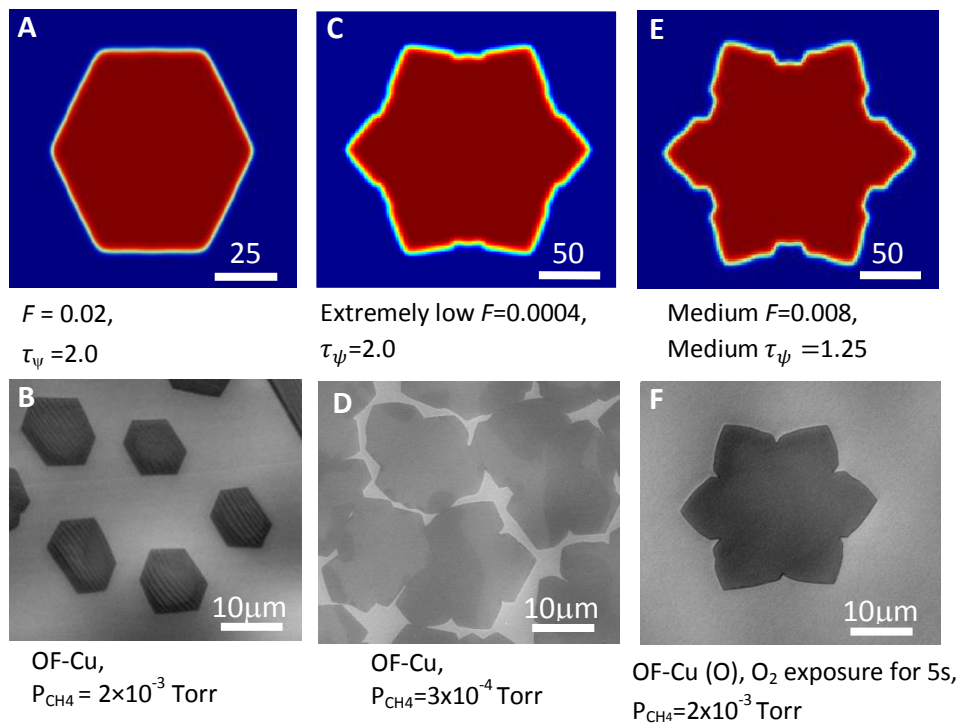


**Fig. S9.**

The comparison between phase field simulations and experimental results. (A, B) The typical hexagonal domain shape on OF-Cu and simulated results. Note that the simulated domain shape is always hexagonal when  $F$  changed from 0.02 to 0.001. (C to F) Transition of domain shapes between edge-attachment-limited growth and diffusion-limited growth. Both show the less compact (or transitional) domain morphologies.

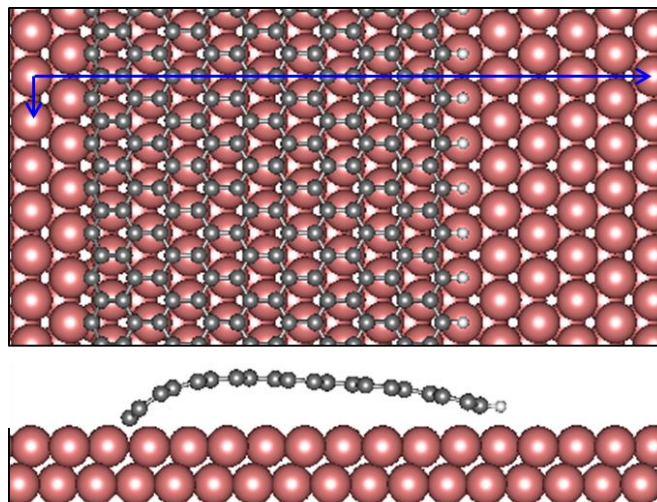


**Fig. S10.**

The structure for modeling graphene edge on Cu(111). The Cu atoms are shown in red, C in grey, and H in white. Top panel is the top view and the bottom one is the side view. The blue arrows denote the supercell vectors.

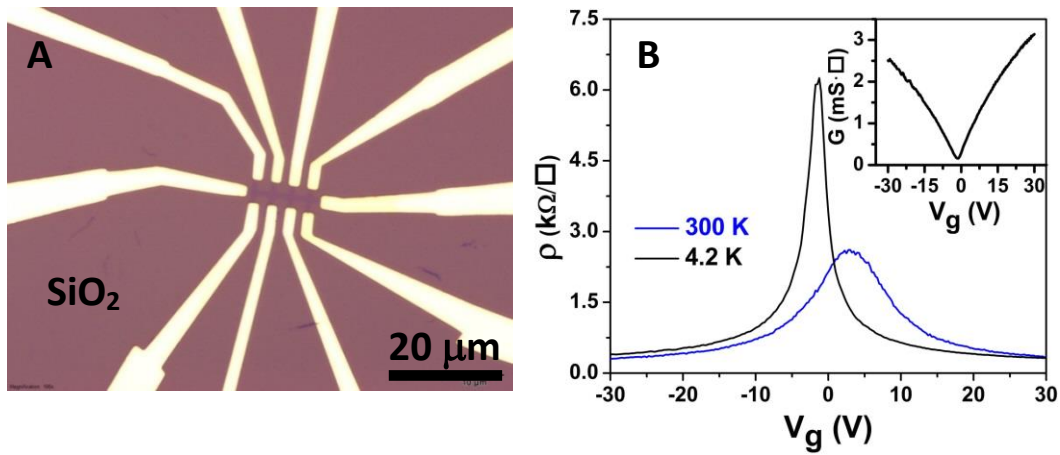


**Fig. S11.**

Electrical transport probed in graphene devices using large graphene domains on SiO<sub>2</sub>/Si substrates. (A) An optical microscopy image of a device on SiO<sub>2</sub>/Si substrate. (B) Transfer characteristics of the device at 4.2K and room temperature, respectively. Inset: conductivity as a function of back gate voltage at 4.2K.

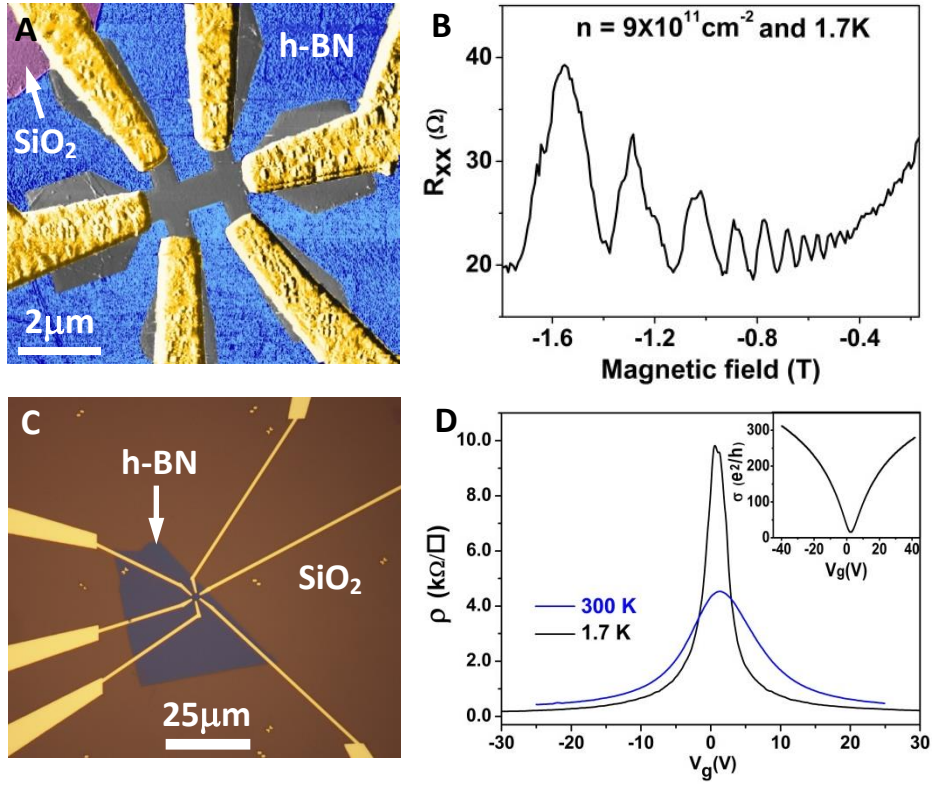


**Fig. S12.**

(A) A false-colored AFM image of a device on h-BN fabricated from a large dendritic graphene domain. (B)  $R_{xx}$  as a function of magnetic field at a fixed carrier density. (C) An optical microscopy image of a device on h-BN fabricated from a small hexagonal graphene domain. (D) Transfer characteristics of the device at 1.7K and 300K, respectively. Inset is the corresponding conductivity as a function of back gate voltage at 1.7K. The extracted carrier mobility (18) is  $50,000 \text{ cm}^2 \text{ V}^{-1} \text{ s}^{-1}$  and  $15,000 \text{ cm}^2 \text{ V}^{-1} \text{ s}^{-1}$  at 1.7K and room temperature, respectively, indicating that the electrical quality of small compact graphene domains is similar to that of large dendritic domains.

## References and Notes

1. X. Li, W. Cai, J. An, S. Kim, J. Nah, D. Yang, R. Piner, A. Velamakanni, I. Jung, E. Tutuc, S. K. Banerjee, L. Colombo, R. S. Ruoff, Large-area synthesis of high-quality and uniform graphene films on copper foils. *Science* **324**, 1312–1314 (2009). [doi:10.1126/science.1171245](https://doi.org/10.1126/science.1171245) [Medline](#)
2. S. Bae, H. Kim, Y. Lee, X. Xu, J.-S. Park, Y. Zheng, J. Balakrishnan, T. Lei, H. Ri Kim, Y. I. Song, Y.-J. Kim, K. S. Kim, B. Özyilmaz, J.-H. Ahn, B. H. Hong, S. Iijima, Roll-to-roll production of 30-inch graphene films for transparent electrodes. *Nat. Nanotechnol.* **5**, 574–578 (2010). [doi:10.1038/nnano.2010.132](https://doi.org/10.1038/nnano.2010.132) [Medline](#)
3. N. C. Bartelt, K. F. McCarty, Graphene growth on metal surfaces. *MRS Bull.* **37**, 1158–1165 (2012). [doi:10.1557/mrs.2012.237](https://doi.org/10.1557/mrs.2012.237)
4. A. W. Tsen, L. Brown, M. P. Levendorf, F. Ghahari, P. Y. Huang, R. W. Havener, C. S. Ruiz-Vargas, D. A. Muller, P. Kim, J. Park, Tailoring electrical transport across grain boundaries in polycrystalline graphene. *Science* **336**, 1143–1146 (2012). [doi:10.1126/science.1218948](https://doi.org/10.1126/science.1218948) [Medline](#)
5. P. M. Ajayan, B. I. Yakobson, Graphene: Pushing the boundaries. *Nat. Mater.* **10**, 415–417 (2011). [doi:10.1038/nmat3027](https://doi.org/10.1038/nmat3027) [Medline](#)
6. S. Bhaviripudi, X. Jia, M. S. Dresselhaus, J. Kong, Role of kinetic factors in chemical vapor deposition synthesis of uniform large area graphene using copper catalyst. *Nano Lett.* **10**, 4128–4133 (2010). [doi:10.1021/nl102355e](https://doi.org/10.1021/nl102355e) [Medline](#)
7. I. Vlassiouk, M. Regmi, P. Fulvio, S. Dai, P. Datskos, G. Eres, S. Smirnov, Role of hydrogen in chemical vapor deposition growth of large single-crystal graphene. *ACS Nano* **5**, 6069–6076 (2011). [doi:10.1021/nn201978y](https://doi.org/10.1021/nn201978y) [Medline](#)
8. Z. Yan, J. Lin, Z. Peng, Z. Sun, Y. Zhu, L. Li, C. Xiang, E. L. Samuel, C. Kittrell, J. M. Tour, Toward the synthesis of wafer-scale single-crystal graphene on copper foils. *ACS Nano* **6**, 9110–9117 (2012). [doi:10.1021/nn303352k](https://doi.org/10.1021/nn303352k) [Medline](#)
9. H. Wang, G. Wang, P. Bao, S. Yang, W. Zhu, X. Xie, W. J. Zhang, Controllable synthesis of submillimeter single-crystal monolayer graphene domains on copper foils by suppressing nucleation. *J. Am. Chem. Soc.* **134**, 3627–3630 (2012). [doi:10.1021/ja2105976](https://doi.org/10.1021/ja2105976) [Medline](#)
10. Z. Zhang, M. G. Lagally, Atomistic processes in the early stages of thin-film growth. *Science* **276**, 377–383 (1997). [doi:10.1126/science.276.5311.377](https://doi.org/10.1126/science.276.5311.377) [Medline](#)
11. Materials and methods are available as supplementary materials on *Science Online*.
12. X. Li, W. Cai, L. Colombo, R. S. Ruoff, Evolution of graphene growth on Ni and Cu by carbon isotope labeling. *Nano Lett.* **9**, 4268–4272 (2009). [doi:10.1021/nl902515k](https://doi.org/10.1021/nl902515k) [Medline](#)
13. S. Nie, J. M. Wofford, N. C. Bartelt, O. D. Dubon, K. F. McCarty, Origin of the mosaicity in graphene grown on Cu(111). *Phys. Rev. B* **84**, 155425 (2011). [doi:10.1103/PhysRevB.84.155425](https://doi.org/10.1103/PhysRevB.84.155425)

14. G. H. Han, F. Güneş, J. J. Bae, E. S. Kim, S. J. Chae, H. J. Shin, J. Y. Choi, D. Pribat, Y. H. Lee, Influence of copper morphology in forming nucleation seeds for graphene growth. *Nano Lett.* **11**, 4144–4148 (2011). [doi:10.1021/nl201980p](https://doi.org/10.1021/nl201980p) [Medline](#)
15. J. Gao, J. Yip, J. Zhao, B. I. Yakobson, F. Ding, Graphene nucleation on transition metal surface: Structure transformation and role of the metal step edge. *J. Am. Chem. Soc.* **133**, 5009–5015 (2011). [doi:10.1021/ja110927p](https://doi.org/10.1021/ja110927p) [Medline](#)
16. H. Chen, W. Zhu, Z. Zhang, Contrasting behavior of carbon nucleation in the initial stages of graphene epitaxial growth on stepped metal surfaces. *Phys. Rev. Lett.* **104**, 186101 (2010). [doi:10.1103/PhysRevLett.104.186101](https://doi.org/10.1103/PhysRevLett.104.186101) [Medline](#)
17. B. Hammer, J. K. Nørskov, Theoretical surface science and catalysis—calculations and concepts. *Adv. Catal.* **45**, 71–129 (2000). [doi:10.1016/S0360-0564\(02\)45013-4](https://doi.org/10.1016/S0360-0564(02)45013-4)
18. E. H. Hwang, S. Adam, S. D. Sarma, Carrier transport in two-dimensional graphene layers. *Phys. Rev. Lett.* **98**, 186806 (2007). [doi:10.1103/PhysRevLett.98.186806](https://doi.org/10.1103/PhysRevLett.98.186806) [Medline](#)
19. N. Petrone, C. R. Dean, I. Meric, A. M. van der Zande, P. Y. Huang, L. Wang, D. Muller, K. L. Shepard, J. Hone, Chemical vapor deposition-derived graphene with electrical performance of exfoliated graphene. *Nano Lett.* **12**, 2751–2756 (2012). [doi:10.1021/nl204481s](https://doi.org/10.1021/nl204481s) [Medline](#)
20. C. R. Dean, A. F. Young, I. Meric, C. Lee, L. Wang, S. Sorgenfrei, K. Watanabe, T. Taniguchi, P. Kim, K. L. Shepard, J. Hone, Boron nitride substrates for high-quality graphene electronics. *Nat. Nanotechnol.* **5**, 722–726 (2010). [doi:10.1038/nnano.2010.172](https://doi.org/10.1038/nnano.2010.172) [Medline](#)
21. E. Starodub, N. C. Bartelt, K. F. McCarty, Oxidation of graphene on metals. *J. Phys. Chem. C* **114**, 5134–5140 (2010). [doi:10.1021/jp912139e](https://doi.org/10.1021/jp912139e)
22. W. Zhang, P. Wu, Z. Li, J. Yang, First-principles thermodynamics of graphene growth on Cu surfaces. *J. Phys. Chem. C* **115**, 17782–17787 (2011). [doi:10.1021/jp2006827](https://doi.org/10.1021/jp2006827)
23. H. Kim, C. Mattevi, M. R. Calvo, J. C. Oberg, L. Artiglia, S. Agnoli, C. F. Hirjibehedin, M. Chhowalla, E. Saiz, Activation energy paths for graphene nucleation and growth on Cu. *ACS Nano* **6**, 3614–3623 (2012). [doi:10.1021/nn3008965](https://doi.org/10.1021/nn3008965) [Medline](#)
24. I. Alstrup, I. Chorkendorff, S. Ullmann, The interaction of CH<sub>4</sub> at high temperatures with clean and oxygen precovered Cu(100). *Surf. Sci.* **264**, 95–102 (1992). [doi:10.1016/0039-6028\(92\)90168-6](https://doi.org/10.1016/0039-6028(92)90168-6)
25. B. Xing, X. Y. Pang, G. C. Wang, C–H bond activation of methane on clean and oxygen pre-covered metals: A systematic theoretical study. *J. Catal.* **282**, 74–82 (2011). [doi:10.1016/j.jcat.2011.05.027](https://doi.org/10.1016/j.jcat.2011.05.027)
26. R. A. van Santen, M. Neurock, S. G. Shetty, Reactivity theory of transition-metal surfaces: A Brønsted–Evans–Polanyi linear activation energy–free-energy analysis. *Chem. Rev.* **110**, 2005–2048 (2010). [doi:10.1021/cr9001808](https://doi.org/10.1021/cr9001808) [Medline](#)
27. V. I. Artyukhov, Y. Liu, B. I. Yakobson, Equilibrium at the edge and atomistic mechanisms of graphene growth. *Proc. Natl. Acad. Sci. U.S.A.* **109**, 15136–15140 (2012). [doi:10.1073/pnas.1207519109](https://doi.org/10.1073/pnas.1207519109) [Medline](#)



28. T. A. Witten, Jr., L. M. Sander, Diffusion-limited aggregation, a kinetic critical phenomenon. *Phys. Rev. Lett.* **47**, 1400–1403 (1981). [doi:10.1103/PhysRevLett.47.1400](https://doi.org/10.1103/PhysRevLett.47.1400)
29. Q. Yu, L. A. Jauregui, W. Wu, R. Colby, J. Tian, Z. Su, H. Cao, Z. Liu, D. Pandey, D. Wei, T. F. Chung, P. Peng, N. P. Guisinger, E. A. Stach, J. Bao, S. S. Pei, Y. P. Chen, Control and characterization of individual grains and grain boundaries in graphene grown by chemical vapour deposition. *Nat. Mater.* **10**, 443–449 (2011). [doi:10.1038/nmat3010](https://doi.org/10.1038/nmat3010) [Medline](#)
30. B. Wu, D. Geng, Z. Xu, Y. Guo, L. Huang, Y. Xue, J. Chen, G. Yu, Y. Liu, Self-organized graphene crystal patterns. *NPG Asia Materials* **5**, e36 (2013). [doi:10.1038/am.2012.68](https://doi.org/10.1038/am.2012.68)
31. A. T. Murdock, A. Koos, T. B. Britton, L. Houben, T. Batten, T. Zhang, A. J. Wilkinson, R. E. Dunin-Borkowski, C. E. Lekka, N. Grobert, Controlling the orientation, edge geometry, and thickness of chemical vapor deposition graphene. *ACS Nano* **7**, 1351–1359 (2013). [doi:10.1021/nn3049297](https://doi.org/10.1021/nn3049297) [Medline](#)
32. J. W. Suk, A. Kitt, C. W. Magnuson, Y. Hao, S. Ahmed, J. An, A. K. Swan, B. B. Goldberg, R. S. Ruoff, Transfer of CVD-grown monolayer graphene onto arbitrary substrates. *ACS Nano* **5**, 6916–6924 (2011). [doi:10.1021/nn201207c](https://doi.org/10.1021/nn201207c) [Medline](#)
33. S. Chen, H. Ji, H. Chou, Q. Li, H. Li, J. W. Suk, R. Piner, L. Liao, W. Cai, R. S. Ruoff, Millimeter-size single-crystal graphene by suppressing evaporative loss of Cu during low pressure chemical vapor deposition. *Adv. Mater.* **25**, 2062–2065 (2013). [doi:10.1002/adma.201204000](https://doi.org/10.1002/adma.201204000) [Medline](#)
34. Y. Hao, Y. Wang, L. Wang, Z. Ni, Z. Wang, R. Wang, C. K. Koo, Z. Shen, J. T. Thong, Probing layer number and stacking order of few-layer graphene by Raman spectroscopy. *Small* **6**, 195–200 (2010). [doi:10.1002/sml.200901173](https://doi.org/10.1002/sml.200901173) [Medline](#)
35. R. Kobayashi, Modeling and numerical simulations of dendritic crystal growth. *Physica D* **63**, 410–423 (1993). [doi:10.1016/0167-2789\(93\)90120-P](https://doi.org/10.1016/0167-2789(93)90120-P)
36. L. Q. Chen, Phase-field models for microstructure evolution. *Annu. Rev. Mater. Res.* **32**, 113–140 (2002). [doi:10.1146/annurev.matsci.32.112001.132041](https://doi.org/10.1146/annurev.matsci.32.112001.132041)
37. A. Karma, M. Plapp, Spiral surface growth without desorption. *Phys. Rev. Lett.* **81**, 4444–4447 (1998). [doi:10.1103/PhysRevLett.81.4444](https://doi.org/10.1103/PhysRevLett.81.4444)
38. [www.fftw.org](http://www.fftw.org)
39. G. Kresse, J. Furthmüller, Efficient iterative schemes for ab initio total-energy calculations using a plane-wave basis set. *Phys. Rev. B* **54**, 11169–11186 (1996). [doi:10.1103/PhysRevB.54.11169](https://doi.org/10.1103/PhysRevB.54.11169) [Medline](#)
40. G. Kresse, J. Hafner, Ab initio molecular dynamics for liquid metals. *Phys. Rev. B* **47**, 558–561 (1993). [doi:10.1103/PhysRevB.47.558](https://doi.org/10.1103/PhysRevB.47.558) [Medline](#)
41. G. Kresse, J. Hafner, Norm-conserving and ultrasoft pseudopotentials for first-row and transition elements. *J. Phys. Condens. Matter* **6**, 8245–8257 (1994). [doi:10.1088/0953-8984/6/40/015](https://doi.org/10.1088/0953-8984/6/40/015)
42. D. Vanderbilt, Soft self-consistent pseudopotentials in a generalized eigenvalue formalism. *Phys. Rev. B* **41**, 7892–7895 (1990). [doi:10.1103/PhysRevB.41.7892](https://doi.org/10.1103/PhysRevB.41.7892) [Medline](#)

- 43. D. M. Ceperley, B. J. Alder, Ground state of the electron gas by a stochastic method. *Phys. Rev. Lett.* **45**, 566–569 (1980). [doi:10.1103/PhysRevLett.45.566](https://doi.org/10.1103/PhysRevLett.45.566)
- 44. M. Vanin, J. J. Mortensen, A. K. Kelkkanen, J. M. Garcia-Lastra, K. S. Thygesen, K. W. Jacobsen, Graphene on metals: A van der Waals density functional study. *Phys. Rev. B* **81**, 081408 (2010). [doi:10.1103/PhysRevB.81.081408](https://doi.org/10.1103/PhysRevB.81.081408)
- 45. H. J. Monkhorst, J. D. Pack, Special points for Brillouin-zone integrations. *Phys. Rev. B* **13**, 5188–5192 (1976). [doi:10.1103/PhysRevB.13.5188](https://doi.org/10.1103/PhysRevB.13.5188)